Check for updates

Chemistry
A European
Journal

Chemistry Europe
European Chemical Societies Publishing

Accepted Article

Title: Metallic-glass films with Nanostructured Periodic Density Fluctuations Supported on Si/SiO2 as Efficient Hydrogen Sorber

Authors: Baran Sarac, Yurii P. Ivanov, Tolga Karazehir, Barbara Putz, A. Lindsay Greer, A. Sezai Sarac, and Jürgen Eckert

This manuscript has been accepted after peer review and appears as an Accepted Article online prior to editing, proofing, and formal publication of the final Version of Record (VoR). This work is currently citable by using the Digital Object Identifier (DOI) given below. The VoR will be published online in Early View as soon as possible and may be different to this Accepted Article as a result of editing. Readers should obtain the VoR from the journal website shown below when it is published to ensure accuracy of information. The authors are responsible for the content of this Accepted Article.

To be cited as: *Chem. Eur. J.* 10.1002/chem.202001596

Link to VoR: https://doi.org/10.1002/chem.202001596

WILEY-VCH

10.1002/chem.202001596

Metallic-glass films with Nanostructured Periodic Density Fluctuations Supported on Si/SiO_2 as Efficient Hydrogen Sorber

Baran Sarac,*[a] Yurii P. Ivanov,[b, c] Tolga Karazehir,[d] Barbara Putz,[a, e]

A. Lindsay Greer,[b] A. Sezai Sarac,[f] and Jürgen Eckert[a, g]

[a] *Dr. B. Sarac, Dr. B. Putz, Prof. J. Eckert*

Erich Schmid Institute of Materials Science, Austrian Academy of Sciences, 8700 Leoben, Austria

E-mail: baransarac@gmail.com

[b] *Dr. Y.P.Ivanov, Prof. A. L. Greer*

Department of Materials Science & Metallurgy, University of Cambridge, Cambridge CB3 0FS, UK

[c] *Dr. Y.P.Ivanov*

School of Natural Sciences, Far Eastern Federal University, 690950, Vladivostok, Russia

[d] *Dr. T. Karazehir*

Department of Energy System Engineering, Adana Alparslan Türkeş Science and Technology University, 01250 Saricam, Adana, Turkey

[e] *Dr. B. Putz*

EMPA - Swiss Federal Laboratories for Materials Science and Technology, 3602, Thun, Switzerland

[f] *Prof. A. Sezai Sarac*

Polymer Science and Technology, Nanoscience & Nanoengineering, Istanbul Technical University, 34469 Istanbul, Turkey

[g] *Prof. J. Eckert*

Department of Materials Science, Chair of Materials Physics, Montanuniversität Leoben, 8700 Leoben, Austria

Supporting Information is available: Experimental Section – Electrochemical Characterization, and Supplementary Figures and Tables

Accepted Manuscript

This article is protected by copyright. All rights reserved.

10.1002/chem.202001596

Nanostructured metallic glass films (NMGF) can exhibit surface and intrinsic effects that give rise to unique physical and chemical properties. Here we report a facile synthesis and electrochemical, structural, and morphologic characterization of Pd-Au-Si based MGs of ~50 nm thickness supported on Si/SiO_2. Impressively, the maximum total hydrogen charge stored in Pd-Au-Si nanofilm is equal to that in polycrystalline Pd films with 1 µm thickness in 0.1 M H_2SO_4 electrolyte. The same NMGF has a volumetric desorption charge that is more than eight times and 25% higher than that of polycrystalline PdNF and Pd-Cu-Si NMGF with the same thickness supported on Si/SiO_2, respectively. A significant number of nanovoids originated from PdH_x crystals, and an increase in average interatomic spacing is detected in Pd-Au-Si NMGF by high-resolution TEM. Such a high amount of hydrogen sorption is linked to the unique density fluctuations without any chemical segregation exclusively observed for this NMGF.

Introduction

It is known that the selected composition at the deep eutectic point and its nearby compositions should have kinetics faster than any of the competing eutectic, and in some situations, the primary phases.[1] Fully amorphous $Pd_{82}Si_{18}$ composition with a deep eutectic can be cast up to 8 mm which is even larger than many other ternary alloys and can be extended to 15 mm with the replacement of small amounts of Pd with Cu.[2] In terms of hydrogen interactions, compared to lattice expansion of the Pd polycrystal nanofilms of the same thickness (50 nm), the calculated maximum H/M=1.56 for $Pd_{79}Si_{16}Cu_5$ MG thin film is around 2.5 times larger.[3] Here, the third element Cu disturbs the symmetry of the PdSi-MGs leading to the formation of new interstitial positions for enhanced hydrogen sorption.[4, 5] In terms of the sorption capacitance

This article is protected by copyright. All rights reserved.

Accepted Manuscript

parameter retrieved from the equivalent circuit modeling (ECM) of the electrochemical impedance spectroscopy (EIS), the value is approximately five times bigger than that of the pristine Pd thin films of the same thickness.[6] Hydrogen intake also changes the electronic structure, rendering asymmetric peaks at Pd $3d_{3/2}$ and $3d_{5/2}$ orbitals.[6] Interestingly, as opposed to the electrocatalytic hydrogen activity deterioration of Pt/C or Mo_2C/C electrodes, $Pd_{40}Ni_{10}Cu_{30}P_{20}$ MG ribbons,[7, 8] nanoporous Pd-Cu-S,[9] Pd-Ru nanoparticles,[10] Pd-Ni-P MG with micro/nano hierarchical porous structure,[8, 11] and Pd-Si-Cu thin films in our previous study [12] shows a remarkable improvement as the number of CV cycles increases. Similar to high entropy alloys,[13-15] Pd-Ni-Si-P MG with hierarchical nanostructures,[8, 16] $Pd_{40}Ni_{10}Cu_{30}P_{20}$ MG ribbons,[7, 8] and nanoporous amorphous Pd-Cu-S [9] show a self-stabilizing behavior under long-term static overpotentials. Furthermore, the interaction of hydrogen atoms within Pd takes place with a minimum activation barrier enabling Pd to catalyze hydrogen sorption and desorption.[17, 18]

This study concerns the development of a novel nanostructured metallic glass film (NMGF) composition by tuning the Au content in a near-eutectic Pd-Si binary glass former, and the electrochemical - cyclic voltammetry (CV), EIS and ECM, structural – X-ray diffraction (XRD) and aberration-corrected high-resolution scanning transmission electron microscopy (HRSTEM), and morphologic – atomic force microscopy (AFM) and field-emission gun scanning electron microscopy (FEG-SEM) characterization of the developed NMGF. Following ref.,[19] the range of compositions were estimated based on the extent of the supercooled liquid region ($\Delta T = T_{\mathrm{g}} - T_{\mathrm{x\_onset}}$, where T_{g} is the glass-transition temperature, $T_{\mathrm{x\_onset}}$ is the onset temperature of crystallization), and the compositions at which single-phase bulk Pd-Si-Au and Pd-Si-Cu metallic glasses can be obtained. Based on these two criteria, three new compositions with Au additions

This article is protected by copyright. All rights reserved.

Accepted Manuscript

to Pd-Si metallic glass nanostructured films (NFs) were generated by DC magnetron sputtering (NF1, NF2, and NF3). $Pd_{79}Si_{16}Cu_5$ NFs showing enhanced electrosorption and electrocatalytic behavior (NF4), as well as polycrystalline PdNF, was also investigated for comparison.[3, 6]

In the NMGF and Si/SiO_2 assembly, the main function of the NMGF is the hydrogen storage via electrosorption using a combinatorial chronoamperometry and cyclic voltammetry. The substrate Si/SiO_2 is chosen due to several reasons. First, a seamless adhesion of the NMGF to the substrate on the atomic-scale is achieved during DC magnetron sputtering. Secondly, according to our observations, Si/SiO_2 is highly robust in the diluted H_2SO_4 environment, even in very long-term exposures. Thirdly, and most important, Si/SiO_2 acts as a barrier for the outer diffusion of the sorbed hydrogen, thus enhancing the volumetric sorption and charge density. The presented comprehensive study provides evidence for the highest amount of surface and volumetric gas storage for the Pd-based electrode assembly developed so far, where the developed Pd NMGF and Si/SiO2 assembly are predicted to be excellent alternative materials for hydrogen energy storage and release systems in the near future.

Results and Discussion

Table 1 gives the theoretical density and surface (Q_{d}) and volumetric desorption charges (Q_{v}) obtained from the CV for each NF electrode. NF1 is selected from a near-eutectic Pd-Si system with a slight replacement of Pd with Au.[19] Further replacement of Pd with Si (NF2) with additional Au (NF3) were analyzed to understand the influence of each or both constituents on electrochemical properties. From the literature findings and our observations confirmed that the further increase of Au led to severe crystallization due to the dramatic drop of the glass forming

This article is protected by copyright. All rights reserved.

Accepted Manuscript

10.1002/chem.202001596

kinetics [19]. Finally, NF4, whose chemical composition was optimized in a previous study (Pd replaced with Cu), was chosen for comparison [6].

Table 1. Comparison of crystalline PdNF and NMGF. The composition of each NMGFs in atomic percent was acquired with the TEM-EDX. The thickness of the nanofilms was measured from the High-angle annular dark-field – scanning transmission electron microscopy (HAADF-STEM) imaging. The theoretical densities were calculated from the elemental densities and atomic percentages. The desorption charge of each electrode (divided by the surface area and volume) was extracted from the corresponding CV curves.

Sample	Composition ($\pm$ 1 at.%)	Thickness ($\pm$ 2 nm)	Theoretical Density ($g\ cm^{-3}$) ($\pm$0.1)	Maximum Surface Desorption Charge Q_d ($mC\ cm^{-2}$) ($\pm$ 0.20)	Maximum Volumetric Desorption Charge Q_v ($C\ cm^{-3}$) ($\pm$ 40)
PdNF		102	12.02	1.04	102
NF1	$Pd_{83}Si_{14}Au_3$	69	10.21	1.37	199
NF2	$Pd_{79}Si_{17}Au_4$	72	10.27	4.26	592
NF3	$Pd_{74}Si_{17}Au_9$	55	10.76	4.62	840
NF4	$Pd_{79}Si_{16}Cu_5$	56	9.88	2.48	443

Three samples, i.e., NF3 with the highest desorption charge, PdNF, and Cu-containing NF4, show clear differences (Figure 1a, b, and 1c). The Bode magnitude lines for NF3 intersect at $f = 1000\ \mathrm{Hz}$ and $|Z| = 45\ \Omega$. For PdNF, the inversion point is at $f = 1000\ \mathrm{Hz}$ and $|Z| = 25\ \Omega$. Furthermore, PdNF reaches to lower $|Z|$ values at lower frequencies. Compared to NF3, Cu

This article is protected by copyright. All rights reserved.

Accepted Manuscript

10.1002/chem.202001596

addition to Pd-Si MG (NF4) shifts f to higher values of $1585\ \mathrm{Hz}$ with a similar $|Z|$ of $43\ \Omega$. The Nyquist diagrams (inset) show the distinct behavior of the three compositions; the largest and smallest drops in the impedance from the double-layer region towards the hydrogen evolution region (HER) are observed for the NF3 and NF4 samples, respectively. Moreover, the point where the second time constant disappears shifts from -160 mV for NF3 to -120 mV for PdNF, and $0\ \mathrm{mV}$ for NF4. Hence, the kinetics and potential range of hydrogen sorption/evolution in 0.1 M H_2SO_4 differs from the behavior of polycrystalline Pd films when small additions of Cu or Au are incorporated into PdSi-MG. When the regions of the linear decrease in $|Z|$ as a function of f is compared, the largest slope is observed for the NF3 sample (0.87), followed by PdNF (0.85) and NF4 (0.76). For the NF3 sample, the characteristic frequency range defining this slope shifts to lower values ($4 - 250\ \mathrm{Hz}$, compared to 25 – 630 Hz for the other two samples). These findings indicate that the change from resistive to capacitive behavior of NF3 during hydrogen sorption happens much faster and at lower frequencies.

To correlate the EIS findings with charge transfer resistance and double layer/sorption capacitance, two equivalent circuit models (ECM) of the evaluated materials were generated. The first circuit model was implemented until the second time constant in the Nyquist plots disappears (ECM 1). The Nyquist plots with a single time constant indicate the hydrogen evolution region (HER), which was modeled by the second circuit (ECM 2). Here, $\mathrm{R1}$ is the solution resistance, $\mathrm{R2}$ the charge transfer resistance, $\mathrm{R3}$ the hydrogen evolution resistance, $\mathrm{Q1}$ the double-layer capacitance, and $\mathrm{Q2}$ the sorption capacitance. Figure 1d depicts the double-layer capacitance C_{dl} the behavior of the electrodes as a function of potential. For the NF1, NF2, and NF3 samples, C_{dl} gives a maximum of around $-50\ \mathrm{mV}$. Hence, compositional variation in the Pd-

This article is protected by copyright. All rights reserved.

Accepted Manuscript

10.1002/chem.202001596

Si-Au system does not alter the potential corresponding to the maximum double layer. On the other hand, the maximum C_{dl} drops from $0.30\ \mathrm{mF\ cm^{-2}}$ to $0.18\ \mathrm{mF\ cm^{-2}}$ as the Au content increases. Another increase for the metallic glass nanofilms is observed below $-200\ \mathrm{mV}$, which is related to the initiation of the hydrogen evolution reaction. For the NF4 sample (Pd-Si-Cu), the maximum sorption peak is almost negligible, and a small hump at around $-50\ \mathrm{mV}$ with a maximum of $0.08\ \mathrm{mF\ cm^{-2}}$ is observed. This finding clearly indicates that the adsorption of H^+ ions and the formation of a molecular dielectric by the polarization of the NF4 surface are less pronounced compared to the other MG films of interest. Interestingly, the polycrystalline Pd nanofilm shows a continuous rise in C_{dl} below $-100\ \mathrm{mV}$, reaching a maximum at $0.35\ \mathrm{mF\ cm^{-2}}$ in the HER region. Nevertheless, no apparent pronounced hump is observed, which could indicate a change in the double-layer kinetics. The detailed explanation of the Bode magnitude (Figure S1 and S2), Nyquist (Figure S3 and S4), and Bode phase plots (Figure S5) for all five samples are given in the Supporting Information.

Figure 1e shows the charge-transfer resistance R_{ct} of the electrodes as a function of potential. R_{ct} corresponds to a merely kinetically-controlled electron transfer between electrode and electrolyte, and can be calculated from the radius of the first semicircle.[20] Although the general trend is a decrease in R_{ct} with the drop of the potential towards the HER region, differences between the profiles and values are noticeable. When the double-layer maxima of the samples are compared, NF1 has much larger R_{ct} (*c.f.* $51000\ \Omega\ \mathrm{cm^{-2}}$ for NF1 and $7640\ \Omega\ \mathrm{cm^{-2}}$ for NF3). For the same sample, a higher R_{ct} is preserved in the HER region. In our previous studies, we have shown that the reduction of the size of the semicircles in the Nyquist plots towards negative potentials is due to the interaction of H^+ ions to form PdH_x in the bulk phase. Thus, for the NF1

This article is protected by copyright. All rights reserved.

Accepted Manuscript

10.1002/chem.202001596

sample, it is highly probable that the adsorbed hydrogen cannot easily diffuse to the inner layers, and shows relatively more resistive behavior compared to the other samples. The polycrystalline Pd nanofilm has a lower R_{ct} with a pronounced resistance at $-100\ \mathrm{mV}$ corresponding to hydrogen sorption. Hence, the charge-transfer resistance due to hydrogen sorption for the metallic glass NFs is less sensitive than for the PdNF. Figure 1f shows the sorption capacitance component, Y_{sp}, of the constant phase element. No clear sorption trend is observed for any sample above $-50\ \mathrm{mV}$. Among NFs, NF3 has the highest sorption- capacitance followed by the PdNF. On the other hand, NF1 shows the lowest Y_{sp} in the hydrogen sorption region. Similar to the literature,[21] the Y_{sp} of all electrodes drops dramatically in the HER region due to the enhanced evolution kinetics. Graphs of charge transfer resistance R_{ct} *vs.* characteristic phase-angle maxima θ_{c}, θ_{c} *vs.* characteristic phase-angle frequency ω_{c} and Bode magnitude $|Z|$ *vs.* ω_{c} are discussed in detail in Figure S6 and EIS of NFs – ESI, see the Supporting Information.

The transition between α-solid solution and β-hydride phases is confirmed by cyclic voltammetry and electrochemical impedance spectroscopy (Figure 2a and b). The steady current density and phase of *Z* above $80\ \mathrm{mV}$ correspond to the α-phase formation with very limited hydrogenation.[6, 21-24] Below this potential, the current density for the desorption peak increases, where the phase of *Z* simultaneously starts to decrease. A small increase followed by a very sharp decrease in current density below $-40\ \mathrm{mV}$ with a corresponding steady decrease in the phase of Z is accounted for by β-hydride formation. The highest amount of hydrogenation in Pd, around 35 times higher than that of the α-phase, as well as 3.33 times higher diffusion coefficient, was previously determined in the β-hydride phase (ratios calculated from ref.[25]). For very negative

This article is protected by copyright. All rights reserved.

Accepted Manuscript

10.1002/chem.202001596

potentials ($-180\ \mathrm{mV}$ and lower), the deviation from the linear decrease in the phase of the *Z* plot marks the initiation of hydrogen evolution.

The XRD results presented in Figure 3 confirm structural modifications by the compositional variation. The $\mathrm{Pd}(111)$ peak located at $40.16°$ for the PdNF becomes the first broad diffraction maximum of the amorphous NFs. Si additions (NF1) shift this maximum to higher values, while an increased Au content shifts the maximum to lower 2θ angles, i.e., its position decreases to 39.76° as the Au content increases (NF3). Similarly, the second broad diffraction maximum shifts to lower angles with increasing Au content. The position of the first broad maximum in the XRD scan of the amorphous material is related to the interatomic distances. Due to its relatively smaller atomic size than that of Au, $5\ \mathrm{at.\%}$ of Cu addition (NF4) shifts the first broad diffraction maximum to higher diffraction angles. The second broad maximum, which is mainly due to the atomic bond interactions between Cu and Pd on the short-range order, is not as pronounced. For the as-sputtered samples, a fully amorphous structure without nanocrystals for all NMGFs is confirmed by HRTEM, and seamless attachment between Si/SiO2 and MG is observed for all the samples (Figure S7 for a representative NF3 sample, see the Supporting Information).

One of the main reasons for the enhanced sorption of NF3 is its smoother surface (Figure 4); the root-mean-square (RMS) roughness is $0.34\ \mathrm{nm}$, which is less than half compared to the other Au-containing alloys (NF1 and NF2). Furthermore, fewer surface defects are observed for NF3 films. The roughness is an order of magnitude larger in NF4 ($3.45\ \mathrm{nm}$) and 3 times larger in PdNF ($1.16\ \mathrm{nm}$). When we also refer to our set of Pd–Si–Cu compositions, using Au instead of Cu promotes surface evenness, and quality (free from irregular bumps, pits, etc.).[6] The FEGSEM

This article is protected by copyright. All rights reserved.

Accepted Manuscript

10.1002/chem.202001596

images of polycrystalline PdNFs show a pronounced roughness whereas amorphous NF3 films have a smooth surface (Figure S8, see the Supporting Information).

The increase in the Q_{d} and Y_{sp} values for NF3 are mainly linked to the replacement of Pd atoms with Au in the right proportions. Figure 5a schematically explains the high abundance of surface-active sites in the NF3 sample. Compared to Pd ($137\ \mathrm{pm}$), the larger atomic size of Au ($144\ \mathrm{pm}$) increases the size of the interstitial sites. This enlargement facilitates diffusion of H^+ ions from the surface to the bulk of the nanofilm and increases the possibility of electrochemical hydrogen entrapment. Moreover, the presence of Au facilitates the orientation and homogenization of the distribution of crystalline sites, which results in the highest desorption capacity. Hence, it can be concluded that an optimized Au concentration while considering a sufficient glass-forming ability to produce fully amorphous thin films can yield a higher number of active sites, i.e., voids between and inside atomic clusters, for hydrogen entrapment. Instead, when a Cu atom with an atomic size of $128\ \mathrm{pm}$ replaces Pd (Figure 5b), the interstitial sites shrink and render the diffusion of H^+ ions from the electrolyte into the bulk NF more challenging. Also, the surface-active area for hydrogen entrapment becomes smaller. Our previous findings for the similar-sized thin films corroborate that NF4 with $5\ \mathrm{at.\%}$ Cu has the highest hydrogen-metal activity registered by CV and EIS, whereas further replacement of Pd with Cu could degrade this activity.[6] For Pd, it has been observed that palladium hydride generally forms by the occupation of octahedral interstitial sites.[26, 27] However, due to the fcc close-packed structure of Pd, the size and number of octahedral sites are small, which limits the amount of hydrogen uptake. A representative illustration of the PdH_x formation and the H_2 evolution on the PdNFs is depicted in Figure 5c.

This article is protected by copyright. All rights reserved.

Accepted Manuscript

Cyclic voltammetry of the samples in 0.1 M H_2SO_4 indicates clear differences between the hydrogen (de)sorption and evolution behavior of NMGF and PdNF electrodes (Figure S9, see the Supporting Information). The asymmetric sorption/desorption profile is typical for Pd electrodes owing to the diffusion of hydrogen into the bulk structure.[28, 29] The desorption charge profiles calculated from the potential-dependent region between the anodic and cathodic scans in terms of volume Q_{v}, and surface area, Q_{d} (inset) are provided in Figure 5d. The maximum Q_{v} and Q_{d} values sorbed until the onset of hydrogen sorption (position estimated from the desorption peak) are tabulated in Table 1. The results highlight that the hydrogen-storage capacity of NF3 is almost 25% higher than that of the NF4. Furthermore, the hydrogenation in the PdNF and NF4 samples starts and finishes earlier at larger potentials. Polycrystalline Pd can absorb only 22.5% as much as the NF3 sample per unit area (Q_{d}). When the volumetric desorption charges, Q_{v}, are compared, $Q_{\mathrm{v\_NF3}} = 840\ \mathrm{C\ cm^{-3}}$ is more than eight times larger than that for the $Q_{\mathrm{v\_PdNF}}$. This value is also almost twice that for the $Q_{\mathrm{v\_NF4}}$ ($443\ \mathrm{C\ cm^{-3}}$) (Table 1). The maximum total hydrogen charge stored in NF3 nanofilm, $Q_{\mathrm{d}} = 4.62\ mC\ cm^{-2}$, is equal to that in Pd films of 1 µm (see Figure 11 in ref. [23]). Moreover, this value is larger than for the Pd and Pd3Co nanoparticles, with sizes of a few nanometers electrocoated on the carbon electrode with the calculated overall surface area of $1.2\ cm^2$, are 0.36 and $0.65\ mC\ cm^{-2}$, respectively.[21]

HAADF-STEM of the NMGF and the corresponding EDX analysis within the accuracy of ±1 at.% confirm the presence and homogenous dispersion of the constituent atoms after hydrogenation (Figure S10, see the Supporting Information). There is no apparent correlation between the dark spots on HAADF images and the composition of the films. The dark spots (present in all samples) correspond to the hydrogenated regions. A seamless attachment between the Si/SiO_2 substrate

This article is protected by copyright. All rights reserved.

Accepted Manuscript

10.1002/chem.202001596

and the PVD-sputtered NMGFs is preserved. The polycrystalline structure of Pd is confirmed by HRTEM (Figure 6a). Similar to our previous findings, the Cu-containing NF4 sample exhibits large nanovoids ($20\ \mathrm{nm}$ or larger) emanating from the Si/SiO_2 substrate and bumps on the surface (Figure S11, see the Supporting Information). On the other hand, nanovoids across the film due to hydrogen sorption are observed for the Au-containing NF1, NF2, and NF3 MGs (Figure 6b).

Differently from the other samples, an enlarged view of NF3 (Figure 7a) shows a pronounced periodic modulation of the HAADF contrast with a wavelength of 1.5 nm (Figure 7b and c). Figure S12 (see the Supporting Information) confirms that these fluctuations already exists in the as-sputtered NMGF. The HAADF contrast can be varied across the sample due to the following reasons: inhomogeneities in the average atomic number, local density, specimen thickness, or diffraction contrast variation. The last two are ruled out due to the homogeneous thickness of the specimen and prepared lamellae for TEM, and amorphous structure of the thin film. Moreover, EDX confirms the even composition throughout the cross-section. On the other hand, Au inhomogeneities can also play a role in the formation of the periodic undulations within the NF3 sample, but the possible composition change is extremely small (below 0.5 at %), which is below the detection limit of the high-resolution EDX mapping. Hence, the modulations do not correlate with composition, but with the nanostructured density fluctuations, which is due to the local topology differences between layers, occurring during the DC magnetron sputtering. The amplitude of the undulations is rather weak (1.5-2.5 % only) but sufficient to be imaged by the HAADF detector. The undulations correspond to a few percent deviations in material density, assuming the linear relationship between the HAADF intensity and the local density change [30].

This article is protected by copyright. All rights reserved.

Accepted Manuscript

10.1002/chem.202001596

No nanovoids are present for the crystalline Pd nanofilm, whereas the voids for NF1-NF3 are on the order of several nanometers. For the NF4 samples, only a few large voids, originating at the interface with Si/SiO_2 substrate, are observed (Figure 7d). The highest number of voids homogeneously dispersed over the cross-section is detected for the NF3 samples after hydrogenation (Figure 7e). When compared to the volumetric content of hydride particles (4.5 ± 0.5 vol.%) of NF4, NF3 has almost twice as large amounts (8.6 ± 0.5 vol.%). The findings corroborate the fact that hydrogen ion inclusions in MGs give rise to nanovoid formation, where the MG composition determines the size-distribution over the film. The population of palladium hydride crystals (PdH_x) around the nanovoids detected in HRTEM images is higher because of the increased surface area of the nanovoid-containing NF3 samples, confirming the high desorption charge obtained from the CV curves (Table 1). Kajita *et al.* and Fukunaga *et al.* explained that Si is the element for constructing trigonal prisms, where the number density of prisms increases with the increase with Si and if any additional second metal inclusion in the PdSi-based MG [4, 31, 32]. However, the crystallization study of Chen & Turnbull [19] using PdSi-MG compositions with Ge, Au, Cu, Ag additions confirmed that the glass formation and thermal stability kinetics depend on the composition optimization per each system. The trigonal prisms construct a cluster structure, and the clusters form random cluster networks; thus, H atoms are supposed to occupy the free volume between the clusters [33]. However, compared to fully amorphous as-sputtered state [6], we have recently proven that hydride crystals on the order of 5 nm are formed [3]. Thus we believe that the hydride is sorbed both in tiny nanocrystals and amorphous clusters surrounding them.

The larger hydrogen-storage capacity is also reflected in the volumetric lattice expansion. The hydrogenated PdNF has a lattice spacing of 0.394 ± 0.001 nm (Figure S13, see the Supporting

This article is protected by copyright. All rights reserved.

Accepted Manuscript

Information), whereas the as-sputtered PdNF is retrieved from the XRD diffractogram is 0.389 ± 0.001 nm, confirming the literature [34]. Thus, compared to the maximum unit lattice of Pd (0.402 ± 0.001 nm found in the literature [35], which can also be confirmed by the small shoulder observed on the left side of the (111) peak of the hydrogenated PdNF in Figure S13 - inset, see the Supporting Information) partial hydrogenation is achieved. The positions of the first diffraction maximum of the as-sputtered NF3 and NF4 nanofilms acquired from XRD analysis correspond to the average interatomic spacing of 0.392 ± 0.001 nm and 0.384 ± 0.001 nm for NF3 and NF4, respectively. The average interatomic spacing in the hydrogenated samples after 15 minutes of CA was calculated as 0.400 ± 0.001 nm and 0.391 ± 0.001 nm, respectively (see Figure S12 and inset for a representative azimuthal profile, see the Supporting Information). Compared to Cu-containing NF4, hydrogenation in the Au-containing NF3 samples results in much larger changes in the average interatomic spacing of atoms (cf. $\Delta V_{\mathrm{NF3}} = 3.76$ Å^3, $\Delta V_{\mathrm{NF4}} = 3.15$ Å^3, and $\Delta V_{\mathrm{PdNF}} = 2.30$ Å^3).

Conclusions

This study describes the synthesis and analysis of a new-generation Pd-based NMGF/Si-SiO_2 hybrid structures which may be suitable as potential electrodes for hydrogen storage and evolution systems. In 0.1 M H_2SO_4, Pd-Si metallic glass (MG) with 9 at.% Au (NF3) exhibits $\sim 25\%$ higher sorption capacitance and $\sim 85\%$ higher surface desorption charge compared to 5 at.% Cu containing Pd-Si MG. When the volumetric desorption charges are compared, the NMGF with highest Au-content has Q_{v} more than eight times that of Pd nanocrystalline films. This value is

This article is protected by copyright. All rights reserved.

Accepted Manuscript

10.1002/chem.202001596

almost twice larger that of NMGF with similar amounts of Cu replacing Pd. A dramatic increase in Q_{v} is observed when Pd content drops below 80 at.%. Au replacing Pd has a higher Q_{v} compared to Cu replacing Pd in similar atomic percent. The highest Q_{v} is obtained when the Au content reaches $9\ \mathrm{at.}\%$, which is linked to the enlargement of the interstitial sites due to the replacement of Pd with a bigger element. The more pronounced PdH_x formation is attributed to evenly-distributed several-nm-sized voids in the NF3 sample containing almost twice as large volume percent compared to the Cu-containing NF4 sample, which contains only a few large nanovoids (~20 nm) emanating from the interface with the Si/SiO_2 substrate. HRTEM and STEM-HAADF analyses evidence that the origin of the excellent hydrogen interactions in Au-containing samples (NF3) with the highest amount of Au (9 at.%) is most likely the nanostructured periodic density fluctuations rendering void formation with similar size and spacing. The periodic undulations occur during the DC magnetron sputtering of the nanofilms and are unique to this NF3 sample without any indication of pronounced compositional fluctuations across the nanofilm. The most substantial changes in the interatomic spacing are observed for the 9 at.% Au-containing NF3 nanofilm. The obtained $Q_{\mathrm{d}} = 4.62\ mC\ cm^{-2}$ from the Pd MGNF – Si/SiO_2 assembly is similar to the free-standing ~1 μm crystalline Pd films, while this value can be an order of magnitude larger compared to nanoparticles of Pd and their alloys per unit area. This production (by DC magnetron-sputtering) and characterization methodology allow for the development of metallic glasses with maximum hydrogen uptake via controllable nanovoid formation.

This article is protected by copyright. All rights reserved.

Accepted Manuscript

Experimental Section

Nanofilm Deposition

Nanofilms (thickness $50 - 100$ nm) were deposited on Si(100)/SiO_2 substrates ($10 \times 10 \times 0.525$ mm^3, p-type boron-doped, ρ = 1 - 20 Ω cm) using a custom-built laboratory-scale unbalanced DC magnetron sputtering system with a base pressure $< 10^{-4}$ Pa. The deposition was performed with 2"-diameter circular targets (Pd, 99.95% purity; Si, 99.999% purity; Au, 99.99% purity) in a confocal arrangement ($120°$ in between). The substrates were rinsed in an ultrasonic bath of ethanol and mounted on a rotatable sample holder with a target-to-substrate distance of 75 mm. Prior to deposition, the targets were sputter-cleaned in pure Ar for 10 s, with closed target shutters to protect the substrates and adjacent targets. The thin films were deposited under an Ar atmosphere with a pressure of 0.4 Pa and no intentional substrate heating. Three different chemical compositions of the films were achieved by adjusting the DC power applied to the individual targets (B09: Si 175 W, Pd 108 W, Au 3 W; B10: Si 175 W, Pd 105 W, Au 7 W; B11: Si 175 W, Pd 100 W, Au 14 W, Pd NF: 105 W). For co-deposition of the NFs, the applied power resulted in a total deposition rate of about 7 nm s^{-1}. The deposition time was fixed for all three NFs at 45 s. Due to the lower deposition rate of pure Pd, the deposition time was increased to 90 s to obtain comparable film thicknesses. The film thicknesses were measured by surface step-height measurements using an optical 3D white-light profilometer (Wyko NT 1000). For this purpose, one side of a substrate was masked with Kapton™-tape, which was removed after deposition to produce a sharp surface step. Profilometry (accuracy ± 5nm) was carried out across the step over areas of 0.5×0.5 mm^2.

Nanofilm Characterization

The composition was analyzed by field-emission gun scanning electron microscopy – X-ray energy dispersive spectroscopy (FEGSEM-EDS) on the microscale. The amorphous structure was confirmed by grazing-incidence X-ray diffraction (GIXRD), where the grazing incidence mode eliminated the peaks of Si or SiO_2 coming from the Si(100) substrate on to which the Pd and MG films were sputtered. Atomic force

This article is protected by copyright. All rights reserved.

Accepted Manuscript

microscopy (AFM) imaging was conducted with a NanoMagnetics Instruments - ezAFM+ in tapping mode using a standard silicon tapping mode cantilever with a nominal tip radius of $10\ \mathrm{nm}$. The scan area of interest was $5\ \times\ 5\ \mu\mathrm{m}^2$ (256×256 pixels), and the scan rate was $1\ \mathrm{Hz}$. The theoretical alloy density D_{M} is calculated from the equation $\frac{1}{D_{\mathrm{M}}} = \frac{\omega_{\mathrm{A}}}{D_{\mathrm{A}}} + \frac{\omega_{\mathrm{B}}}{D_{\mathrm{B}}} + \frac{\omega_{\mathrm{C}}}{D_{\mathrm{C}}}$. Here, D_{A}, D_{B} and D_{C} are the densities of A, B, and C, respectively. ω_{A}, ω_{B} and ω_{C} are the mass fractions of A, B, and C in the mixture, respectively, where $\omega_{\mathrm{A}} + \omega_{\mathrm{B}} + \omega_{\mathrm{C}} = 1$. For TEM investigations, cross-sectional specimens were prepared by a focused ion beam (FIB) protocol on a Helios NanoLab DualBeam microscope equipped with a field-emission gun (FEG) electron source and a high-resolution ion column. For the FIB sample preparation, a protective Pt layer was deposited on the samples after hydrogenation. In order to obtain high-quality TEM specimens with no post-induced crystallization, ion milling was carried out under low-voltage conditions. HRTEM studies were performed on a Tecnai Osiris S/TEM (FEI, Netherlands) equipped with a high-brightness gun, Super-X windowless energy dispersive X-ray (EDX) detector system with SDD technology and Gatan Quantum GIF (Gatan, USA). Imaging and spectroscopy studies were performed at 200 kV. The thickness of the areas of interest was estimated from zero-loss EEL spectrum imaging. HRTEM images were analyzed using custom DigitalMicrograph scripts based on the evaluation of the local autocorrelation function.[36] The average volume expansion of NMGFs, $\Delta V = V_{\mathrm{NFH_x}} - V_{\mathrm{NF}}$ was calculated from the difference in the volume of the hydrided ($V_{\mathrm{NFH_x}}$) and as-sputtered (V_{NF}) films.

Electrochemical Nanofilm Hydrogenation

Electrochemical impedance spectroscopy (EIS) of NFs and subsequent electrochemical circuit modeling (ECM) provided the double-layer and sorption capacitance, as well as the charge transfer resistance of each electrode. Prior to measurements, samples were chronoamperometrically hydrogenated at a potential (10 mV) above the hydrogen evolution reaction region for 900 s, where the current stabilization indicating a full saturation is reached within 150 s for all samples. The potential scans were performed from 200 mV to -300 mV, covering the entire range of the hydrogen interactions with the electrode. The

This article is protected by copyright. All rights reserved.

Accepted Manuscript

frequency range was $0.1 - 10000$ Hz at an amplitude of 5 mV. The scans were performed from 0.4 V to -1.2 V, covering the entire hydrogen interactions. Cyclic voltammograms (CV) subsequently recorded between 0 V and 0.6 V at sweep rates of $10\ \mathrm{mV\ s^{-1}}$ depicted the sorption-desorption profile of the NF electrodes. All potentials in this study are given with respect to Ag/AgCl (3M NaCl), where its redox potential is $+0.209$ V *vs.* a standard hydrogen electrode at $25\ ^{\circ}\mathrm{C}$. Hydrogen oxidation (a.k.a. desorption) charges were estimated by integrating the area below the CV curve from 0.4 V to different potentials until the start of hydrogen sorption, according to ref. [23].

Acknowledgements

The authors thank C. Mitterer and V. Terziyska for providing the sputtering device for synthesizing the MG and Pd nanofilms. This work was supported by the European Research Council under the Advanced Grants "INTELHYB – Next generation of complex metallic materials in intelligent hybrid structures" (Grant ERC-2013-ADG-340025), "ExtendGlass – Extending the range of the glassy state: Exploring structure and property limits in metallic glasses" (Grant ERC-2015-ADG-695487), the Austrian Science Fund (FWF) under project grant I3937-N36, and grant 0657-2020-0005 of the Ministry of Science and Higher Education (Russia).

Conflict of Interest

Authors declare no competing financial interest.

Keywords: Thin films, metallic glass, nanostructures, electrosorption, hydrogenation

This article is protected by copyright. All rights reserved.

Accepted Manuscript

References

[1] Y. Li, *JOM*. **2005**, *57*, 60-63.

[2] X. T. Wang, M. Zeng, N. Nollmann, G. Wilde, Z. Tian, C. Y. Tang, *AIP Adv.* **2017**, *7*, 095108

[3] B. Sarac, Y. P. Ivanov, T. Karazehir, M. Mühlbacher, B. Kaynak, A. L. Greer, A. S. Sarac, J. Eckert, *Mater. Horiz.* **2019**, *6*, 1481-1487.

[4] S. Kajita, S. Yamaura, H. Kimura, A. Inoue, *Mater. Trans.* **2010**, *51*, 2133-2138.

[5] S. Kajita, S. Kohara, Y. Onodera, T. Fukunaga, E. Matsubara, *Mater. Trans.* **2011**, *52*, 1349-1355.

[6] B. Sarac, T. Karazehir, M. Mühlbacher, B. Kaynak, C. Gammer, T. Schöberl, A. S. Sarac, J. Eckert, *ACS Appl. Energy Mater.* **2018**, *1*, 2630-2646.

[7] Y. C. Hu, Y. Z. Wang, R. Su, C. R. Cao, F. Li, C. W. Sun, Y. Yang, P. F. Guan, D. W. Ding, Z. L. Wang, W. H. Wang, *Adv. Mater.* **2016**, *28*, 10293-10297.

[8] Y. C. Hu, C. X. Sun, C. W. Sun, *Chemcatchem*. **2019**, *11*, 2401-2414.

[9] W. Xu, S. Zhu, Y. Liang, Z. Cui, X. Yang, A. Inoue, H. Wang, *J. Mater. Chem. A*. **2017**, *5*, 18793-18800.

[10] J. T. Tian, W. Wu, Z. H. Tang, Y. Wu, R. Burns, B. Tichnell, Z. Liu, S. W. Chen, *Catalysts*. **2018**, *8*, 329.

[11] S. S. Wang, N. Li, L. Liu, *Mater. Lett.* **2018**, *228*, 443-446.

[12] B. Sarac, T. Karazehir, M. Mühlbacher, A. S. Sarac, J. Eckert, *Electrocatalysis*. **2020**, *11*, 94-109.

This article is protected by copyright. All rights reserved.

Accepted Manuscript

[13] Z. Y. Ding, J. J. Bian, S. Shuang, X. D. Liu, Y. C. Hu, C. W. Sun, Y. Yang, *Adv. Sustainable Syst.* **2020**.

[14] S. Y. Li, X. W. Tang, H. L. Jia, H. L. Li, G. Q. Xie, X. J. Liu, X. Lin, H. J. Qiu, *J. Catal.* **2020**, *383*, 164-171.

[15] V. Zadorozhnyy, B. Sarac, E. Berdonosova, T. Karazehir, A. Lassnig, C. Gammer, M. Zadorozhnyy, S. Ketov, S. Klyamkin, J. Eckert, *Int. J. Hydrogen Energy*. **2020**, *45*, 5347-5355.

[16] S. H. Gao, J. L. Jia, S. Q. Chen, H. W. Luan, Y. Shao, K. F. Yao, *RSC Adv.* **2017**, *7*, 27058-27064.

[17] W. M. Bartczak, J. Stawowska, *Struct. Chem.* **2004**, *15*, 447-459.

[18] H. Nakatsuji, M. Hada, *J. Am. Chem. Soc.* **1985**, *107*, 8264-8266.

[19] H. S. Chen, D. Turnbull, *Acta Metall.* **1969**, *17*, 1021-1031.

[20] "Gamry Instruments - Basics of Electrochemical Impedance Spectroscopy". Avaliable from https://www.gamry.com/application-notes/EIS/basics-of-electrochemical-impedance-spectroscopy/. (accessed 05/02/2019).

[21] R. K. Singh, R. Ramesh, R. Devivaraprasad, A. Chakraborty, M. Neergat, *Electrochim. Acta*. **2016**, *194*, 199-210.

[22] M. Łukaszewski, K. Hubkowska, U. Koss, A. Czerwiński, *Materials*. **2013**, *6*, 4817-4835.

[23] C. Gabrielli, P. P. Grand, A. Lasia, H. Perrot, *J. Electrochem. Soc.* **2004**, *151*, A1937-A1942.

[24] F. A. Lewis, *Platinum Met. Rev.* **1960**, *4*, 132-137.

[25] P. Millet, M. Srour, R. Faure, R. Durand, *Electrochem. Commun.* **2001**, *3*, 478-482.

[26] R. Caputo, A. Alavi, *Mol. Phys.* **2003**, *101*, 1781-1787.

[27] L. L. Jewell, B. H. Davis, *Appl. Catal., A*. **2006**, *310*, 1-15.

[28] L. Xiao, L. Zhuang, Y. Liu, J. T. Lu, H. D. Abruna, *J. Am. Chem. Soc.* **2009**, *131*, 602-608.

This article is protected by copyright. All rights reserved.

Accepted Manuscript

[29] H. X. Zhang, C. Wang, J. Y. Wang, J. J. Zhai, W. B. Cai, *J. Phys. Chem. C*. **2010**, *114*, 6446-6451.

[30] C. Liu, V. Roddatis, P. Kenesei, R. Maass, *Acta Mater.* **2017**, *140*, 206-216.

[31] Y. Nishi, N. Kayama, S. Kiuchi, K. Suzuki, T. Masumoto, *J. Jpn. Inst. Met.* **1980**, *44*, 1336-1341.

[32] T. Fukunaga, K. Suzuki, *Sci. Rep.* . **1981**, *29*, 153-175.

[33] T. Takeuchi, D. Fukamaki, H. Miyazaki, K. Soda, M. Hasegawa, H. Sato, U. Mizutani, T. Ito, S. Kimura, *Mater. Trans.* **2007**, *48*, 1292-1298.

[34] B. N. Dutta, B. Dayal, *Phys. Status Solidi*. **1963**, *3*, 2253-2259.

[35] A. Maeland, T. B. Flanagan, *J. Phys. Chem.* **1964**, *68*, 1419-1426.

[36] M. Seyring, X. Y. Song, A. Chuvilin, U. Kaiser, M. Rettenmayr, *J. Mater. Res.* **2009**, *24*, 342-346.

[37] B. Sarac, Y. P. Ivanov, A. Chuvilin, T. Schöberl, M. Stoica, Z. Zhang, J. Eckert, *Nat. Commun.* **2018**, *9*, 1333.

Accepted Manuscript

This article is protected by copyright. All rights reserved.

10.1002/chem.202001596

List of Figures

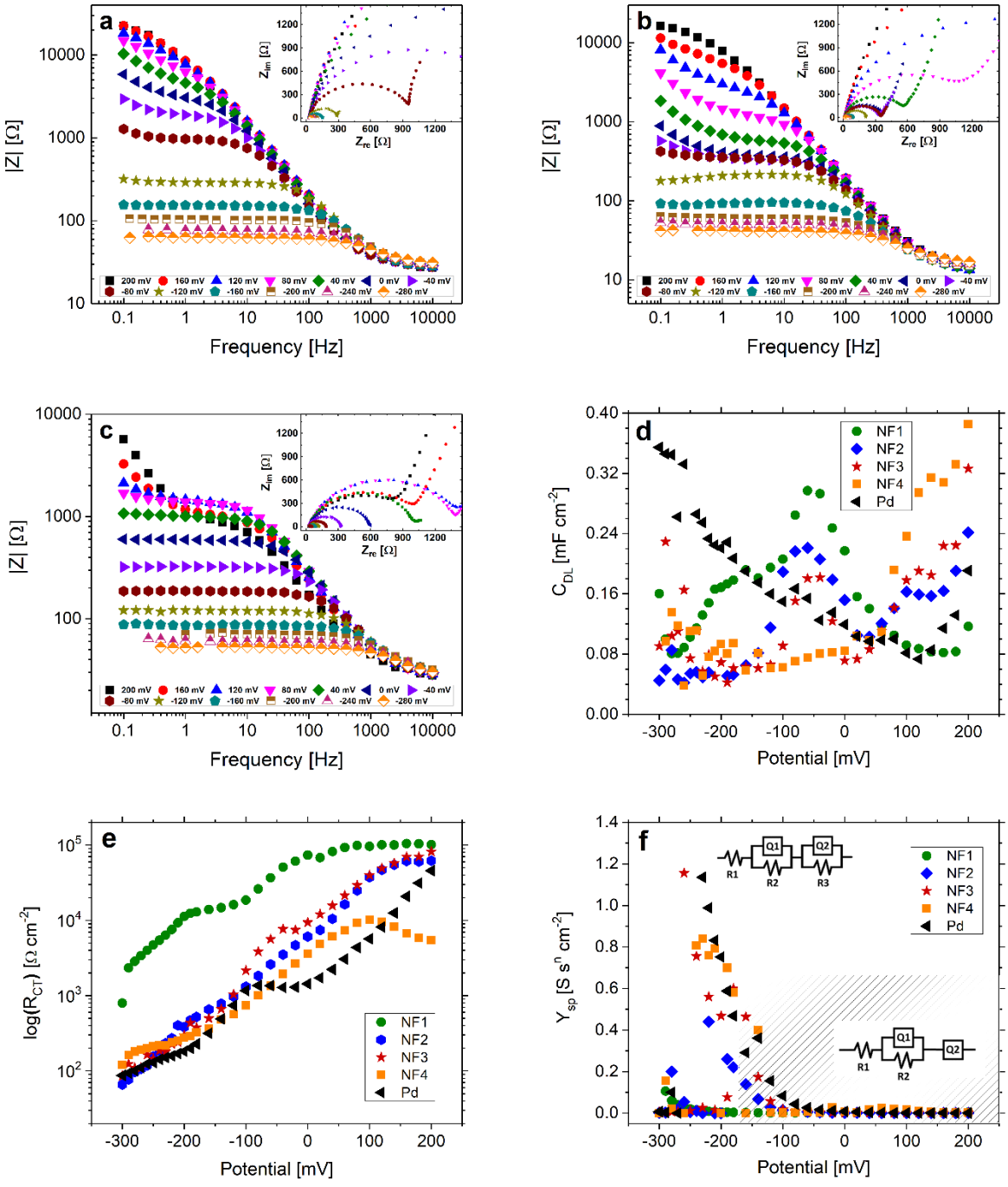

This article is protected by copyright. All rights reserved.

Accepted Manuscript

10.1002/chem.202001596

Figure 1. Bode magnitude and Nyquist (insets) diagrams for (a) NF3, (b) PdNF, and (c) NF4 samples. Variation of the (d) double-layer capacitance, (e) charge-transfer resistance, (f) sorption capacitance as a function of the applied potential.

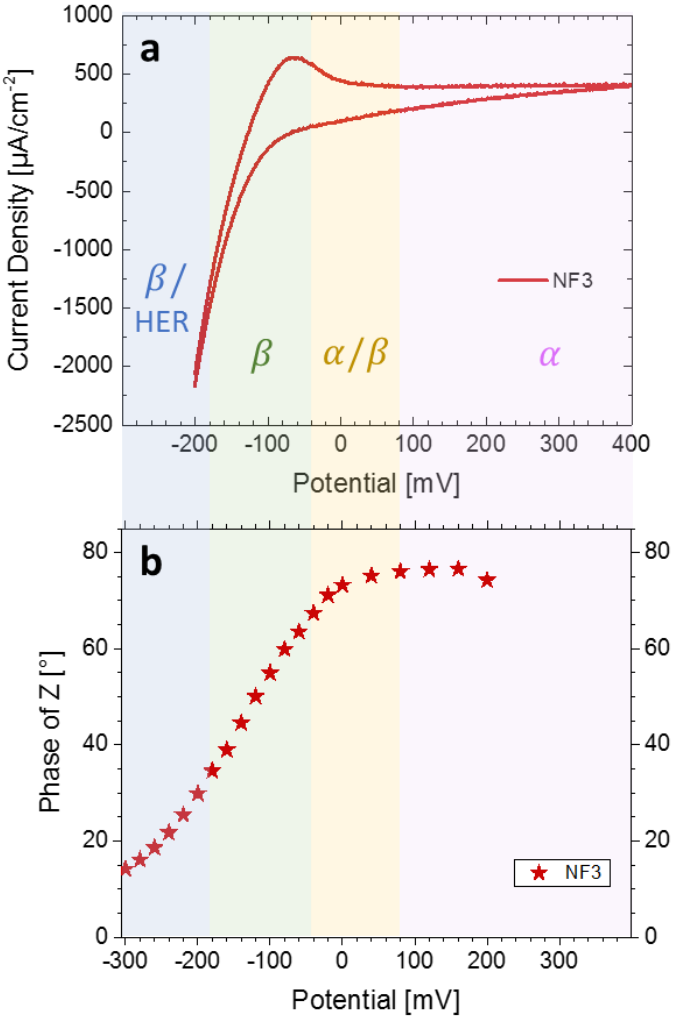

Figure 2. $\alpha -$ solid solution to $\beta -$ hydride phase transition in terms of a decrease in applied potential determined by (a) CV and (b) EIS – θ_c of Bode phase plots.

This article is protected by copyright. All rights reserved.

Accepted Manuscript

10.1002/chem.202001596

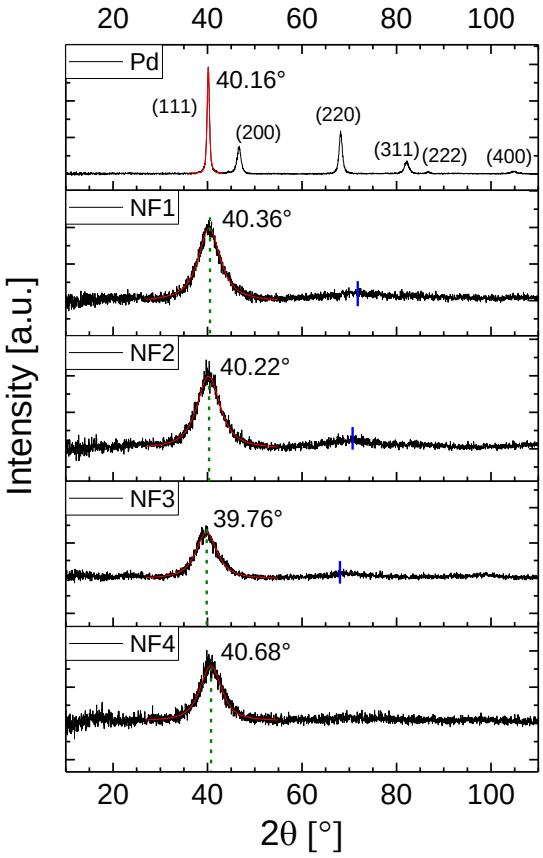

Figure 3. XRD structural characterization of PdNF, NF1, NF2, NF3, and NF4 samples. Green dashed lines are drawn to indicate the diffraction maximum for each composition. Blue ticks indicate the maximum of the second broad peak. The positions of the maxima for the samples except PdNF were determined by fitting to a pseudo-Voigt function, whereas for Pd peaks, a Pearson VII fitting function was used. The indexed Pd peaks corroborate the measurement accuracy within $0.02°$.

Accepted Manuscript

This article is protected by copyright. All rights reserved.

10.1002/chem.202001596

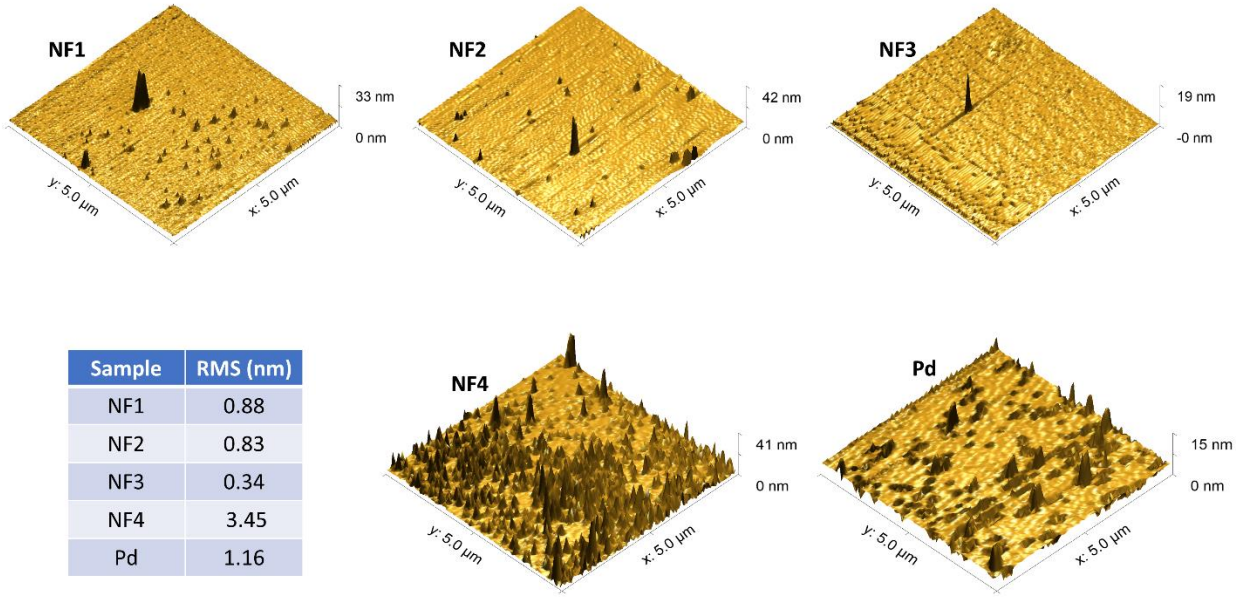

Sample	RMS (nm)
NF1	0.88
NF2	0.83
NF3	0.34
NF4	3.45
Pd	1.16

Figure 4. AFM profiles obtained from representative $5 \times 5\ \mu m^2$ areas. The RMS roughness of each composition is provided in the inset table. All Au-containing NMGFs have roughness lower than 1 nm, whereas the Cu-containing NMGFs have remarkably higher roughness.

Accepted Manuscript

This article is protected by copyright. All rights reserved.

10.1002/chem.202001596

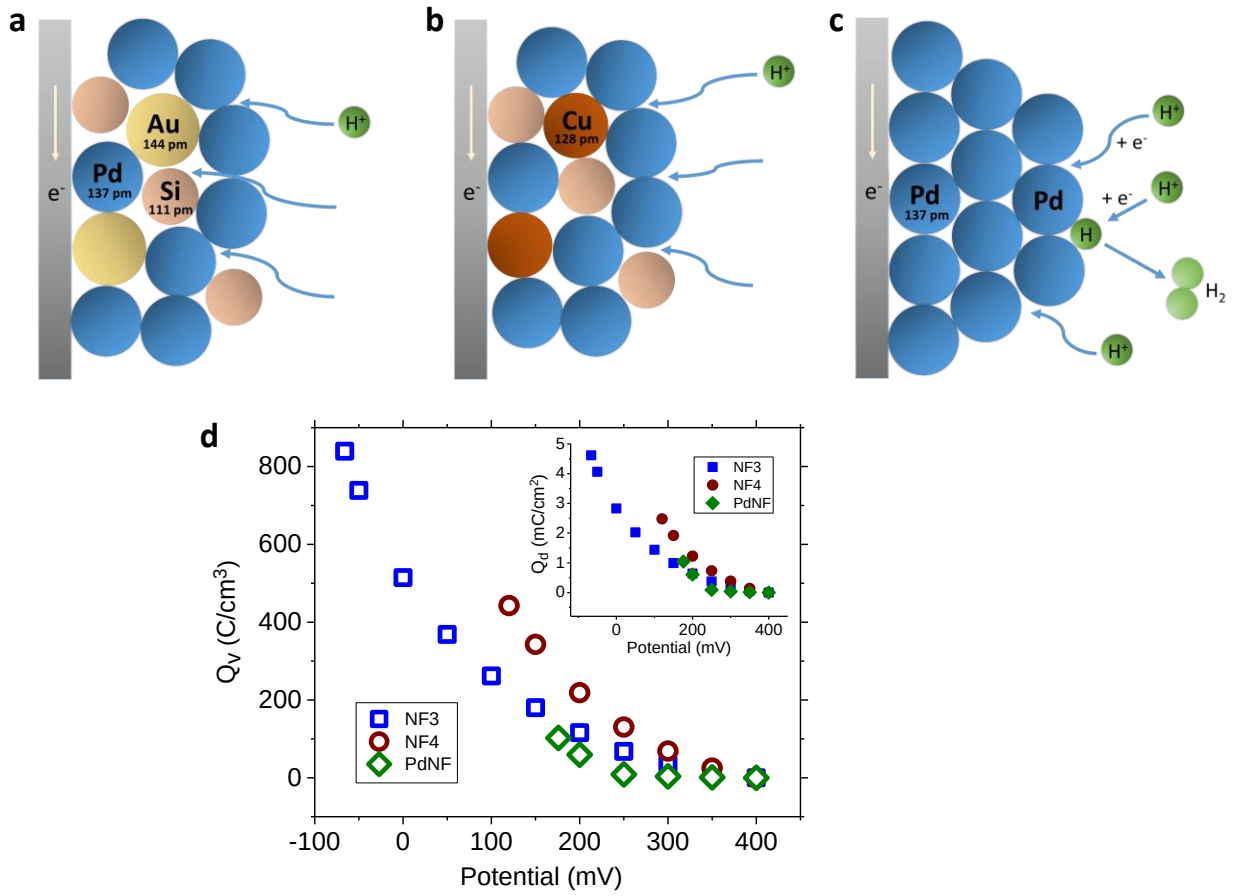

Figure 5. Schematic representation of (a) NF3, (b) NF4, and (c) PdNF electrodes. The hydrogen interaction with Pd and H_2 formation is shown in (c). (d) Increase in volumetric charge Q_v plotted against the potential. The inset shows the charge density Q_d as a function of potential.

Accepted Manuscript

This article is protected by copyright. All rights reserved.

10.1002/chem.202001596

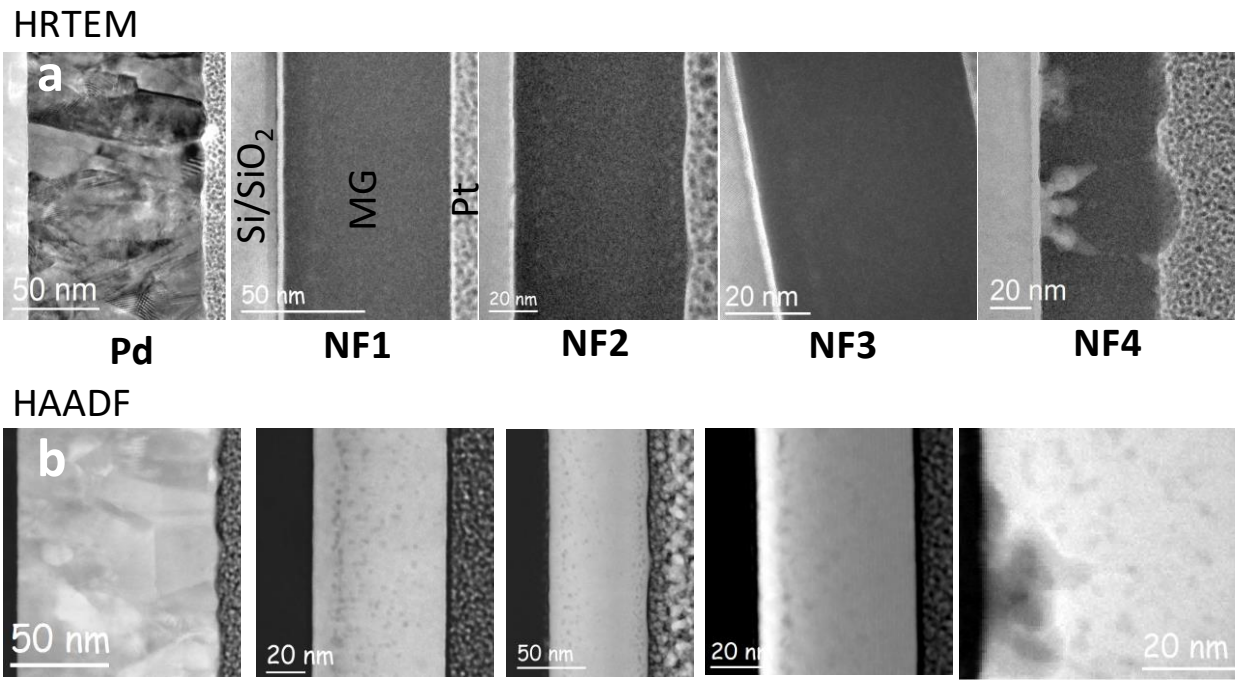

Figure 6. (a) HRTEM and (b) HAADF imaging of crystalline Pd and NMGFs recorded after full saturation with hydrogen.

Accepted Manuscript

This article is protected by copyright. All rights reserved.

10.1002/chem.202001596

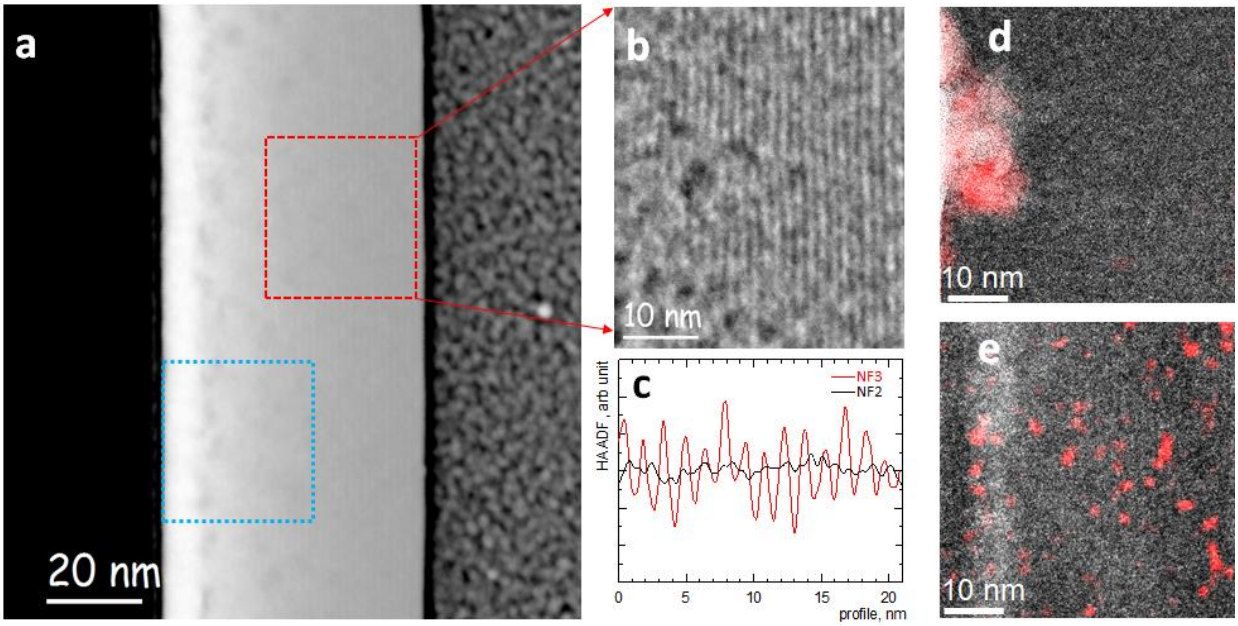

Figure 7. (a) HAADF image of NF3 (white region). Dark spots on the order of several nanometers are voids formed due to hydrogenation (b) Enlarged HAADF view of the periodic undulations in the area shown in (a) by the red dashed square. (c) Linear profiles across the thickness of NF2 and NF3 NFs showing pronounced modulations of the HAADF contrast due to nanostructured density fluctuations in NF3 nanofilms (wavelength 1.5 nm). (d) – (e) Mapping of the local atomic arrangement retrieved by autocorrelation analysis of the HRTEM image (similar to ref.[37]). The pink color indicates regions that are more ordered than the matrix with observable local atomic fringes. (d) The Cu-containing NF4 samples contain large nanovoids of around 20 nm, whereas (e) the Au-containing NF3 samples taken from the blue region in (a) have homogenously distributed voids several nanometers in diameter.

Accepted Manuscript

This article is protected by copyright. All rights reserved.

10.1002/chem.202001596

Table of Contents

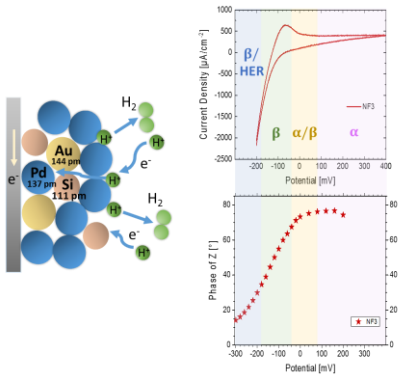

Efficient hydrogen storage and release using new-generation nanostructured metallic glass films (NMGFs) offer green solutions for nano-scale energy applications. This study introduces Pd-Au-Si based metallic glass with unique atomic density fluctuations sputtered on a Si/SiO_2 electrode and their electrochemical, structural, and morphologic properties.

Keywords: Thin films, metallic glass, nanostructures, electrosorption, hydrogenation

Accepted Manuscript

This article is protected by copyright. All rights reserved.